

Article

Effect of Terbium Ion Substitution in Inverse Spinel Nickel Ferrite: Structural and Magnetic Study

Deepa Guragain ^{1,*}, Binod Kumar Rai ² , Sunghyun Yoon ³, Tej Prasad Poudel ¹, Subash Chandra Bhandari ¹ and Sanjay R Mishra ¹

- ¹ Department of Physics, The University of Memphis, Memphis, TN 38152, USA; tejendrapoudel45@gmail.com (T.P.P.); scbhdri@memphis.edu (S.C.B.); srmishra@memphis.edu (S.R.M.)
² Materials Science and Technology Division, Oak Ridge National Laboratory, Oak Ridge, TN 37381, USA; binod4rai@gmail.com
³ Department of Physics, Kunsan National University, Gunsan 573-701, Korea; shyoon@kunsan.ac.kr
* Correspondence: dgragain@memphis.edu or ddeepag13@gmail.com

Received: 30 January 2020; Accepted: 2 March 2020; Published: 10 March 2020



Abstract: Doping rare-earth ions into spinel ferrites can alter their electrical and magnetic properties. The present study delineates the structure–property relationship of the effect of rare-earth terbium doping in NiFe₂O₄ ferrite. X-ray diffraction analysis (XRD) showed unit cell lattice expansion with increased Tb³⁺ content. The Fourier transform infrared spectroscopy (FTIR) results indicate preferential occupancy of Tb³⁺ at the octahedral B site. The magnetic parameters derived from room temperature hysteresis loops where both the saturation magnetization, *M_s*, and coercivity, *H_c*, value decreased with the Tb³⁺ substitution and reached a minimum value of *M_s* ~30.6 emu/g at *x* = 0.1 and *H_c* ~102 Oe at *x* = 0.075. The temperature-dependent magnetocrystalline anisotropy derived from the magnetic isotherm was observed to be the highest for *x* = 0.1 at 5 K with the value *K₁* ~1.09 × 10⁶ J/m³. The Tb³⁺ doping also resulted in the Curie temperature reduction from 938 K at *x* = 0.0 to 899 K at *x* = 0.1.

Keywords: nickel ferrite; spinel; coercivity; isotherm; rare-earth ion

1. Introduction

Nickel ferrite (NiFe₂O₄) with a spinel structure has the general formula AB₂O₄ [1], where all Ni ions are located at the B (Octahedral) site, and iron ions are at both the A (Tetrahedral) and B sites [2]. Nickel ferrite is highly used in electronic devices due to its large permeability at high frequency, low cost, chemical stability, higher electric resistivity, and higher mechanical hardness [3]. The magnetic and dielectric properties of NiFe₂O₄ are highly dependent on the cation distribution, which in turn are strongly dependent on the preparation method [4–7]. Different types of magnetic [8,9] and nonmagnetic atoms for cations [10–15] have been explored to create atomic-level changes in ferrites. This selection affects the Fe³⁺–O²⁻–Fe³⁺ interaction, which changes the crystal structure of ferrites and hence the magnetic properties of the compound [16].

The crystal structure of NiFe₂O₄ is face-centered, where the unit cell contains 32 O²⁻, 8 Ni²⁺, and 16 Fe³⁺ ions, where oxygen ions form 64 tetrahedral and 32 octahedral sites, and 24 cations are distributed [17]. Octahedral and tetrahedral sites are populated with eight Fe³⁺ ions each, and eight Ni²⁺ cations occupy half of the octahedral sites [18]. The bulk NiFe₂O₄ is a familiar inverse spinel with the Ni ion occupying the B site with structure (Fe³⁺_{1-δ})_A[Ni²⁺_δFe³⁺_{1+δ}]_B, while at the nanoscale, the mixed spinel structure of NiFe₂O₄ with Ni²⁺ ions occupying both A- and B-sites was observed.

Aside from replacing Fe³⁺ ions with magnetic and non-magnetic ions, researchers have studied the substitution of rare-earth elements [16,19,20]. Larger ionic radii of the rare-earth ions compared to

Fe^{3+} were observed to bring lattice expansion in ferrites, which can alter the superexchange interaction of $\text{Fe}^{3+}-\text{O}^{2-}-\text{Fe}^{3+}$ [21]. It has been observed that the substitution of rare-earth elements such as Nd^{3+} , Gd^{3+} , Ho^{3+} , Er^{3+} , Tm^{3+} , Y^{3+} , and Lu^{3+} decreases the Curie temperature [16,20,22] compared to pure ferrites, and become more useful for magneto-optical recording [20,23]. Additionally, the substitution of rare-earth ions at the octahedral site affects the hole transfer rate between Ni^{2+} and Ni^{3+} , which increases the electrical resistivity of the compound and hence enables its high-frequency application.

To the best of our knowledge, scant reports are available in the literature on the structural and magnetic properties of Tb^{3+} doped NiFe_2O_4 ferrite nanoparticles. Tb^{3+} was chosen for the substitution, specifically to understand its effect on the magnetic properties of NiFe_2O_4 as Tb^{3+} ions present a large Bohr magneton number, $\mu_{\text{eff}} = 9.7\text{--}9.8$, higher than Gd^{3+} ($\mu_{\text{eff}} = 7.8\text{--}7.9$) [24]. Thus, the presence of Tb^{3+} can greatly alter the A–B site interaction via $\text{Fe}^{3+}-\text{O}^{2-}-\text{Fe}^{3+}(\text{Tb}^{3+})$ interaction. Considering the importance of the substituted NiFe_2O_4 , we report the synthesis of the Tb^{3+} doped $\text{NiFe}_{2-x}\text{Tb}_x\text{O}_4$ ($0.0 \leq x \leq 0.1$) ferrite nanoparticles via the sol-gel method. The experimental results show an increase in the lattice parameter along with the reduction of crystalline size, Curie temperature, magnetization, and coercivity upon Tb^{3+} substitution.

2. Experimental

Terbium doped $\text{NiFe}_{2-x}\text{Tb}_x\text{O}_4$ ($x = 0.00, 0.025, 0.05, 0.075, \text{ and } 0.1$) were prepared via the sol-gel method [25]. Nitrate precursors viz. nickel nitrate hexahydrate, ferric nitrate hexahydrate, and terbium nitrate hexahydrate were used for the synthesis of $\text{NiFe}_{2-x}\text{Tb}_x\text{O}_4$. A homogenous mixture was prepared by mixing a stoichiometric amount of precursor in 10 mL of ethylene glycol and stirred for 30 min at room temperature. A dry gel was obtained by heating the mixture at 70°C for 4 h. Subsequently, the gel was dried in a furnace at 120°C for 3 h. The as-obtained dry gel was later ground and calcined at 600°C for 3 h in a box furnace. The structural and phase analysis of samples was performed using an X-ray diffractometer (XRD), where the patterns were collected using $\text{Cu K}\alpha$ radiation in the $2\theta = 25\text{--}70^\circ$ range at a step size of 0.0485 and acquisition time of 0.2 s. The room temperature magnetic properties of the samples were investigated using a vibrating sample magnetometer (VSM). Additionally, magnetic isotherms were obtained in the field of ± 60 kOe and in the temperature range of 5–300 K via SQUID (Quantum Design). The infrared spectrum of samples was collected using the Fourier transfer infrared spectrometer (FTIR, Thermo Nicolet iS 10). The Curie (Neel) temperature (T_c) of the samples was measured using a modified thermogravimetric analyzer (TGA, Instrument Specialists Inc., Memphis, USA) equipped with a permanent magnet.

3. Results and Discussion

Figure 1a shows the XRD pattern of the calcined $\text{NiTb}_x\text{Fe}_{2-x}\text{O}_4$ ($x = 0.00, 0.025, 0.05, 0.075, \text{ and } 0.1$) ferrites. All the Tb^{3+} substituted nickel ferrites showed a single-phase spinel structure. No impurity peaks were detected within the detection limit of the instrument. Table 1 shows that the lattice parameter “ a ” for $\text{NiTb}_x\text{Fe}_{2-x}\text{O}_4$ linearly increased with the Tb^{3+} content. The increase in the lattice parameter upon Tb^{3+} substitution was due to the larger Tb^{3+} ions (ionic radii ~ 0.923 Å) replacing Fe^{3+} ions (ionic radii ~ 0.645 Å). The X-ray density was calculated using the relation [26]: $\rho_x = 8M/N_A a^3$, where M is the relative molecular mass, N_A is the Avogadro’s number, and ‘ a ’ is the lattice parameter. The multiplication factor 8 was used as there is an 8-formula unit in a unit cell. Table 1 shows that the X-ray density increases with the Tb^{3+} content. This is because the molecular mass increased with the increase in the Tb^{3+} content due to the higher atomic weight of Tb than that of Fe.

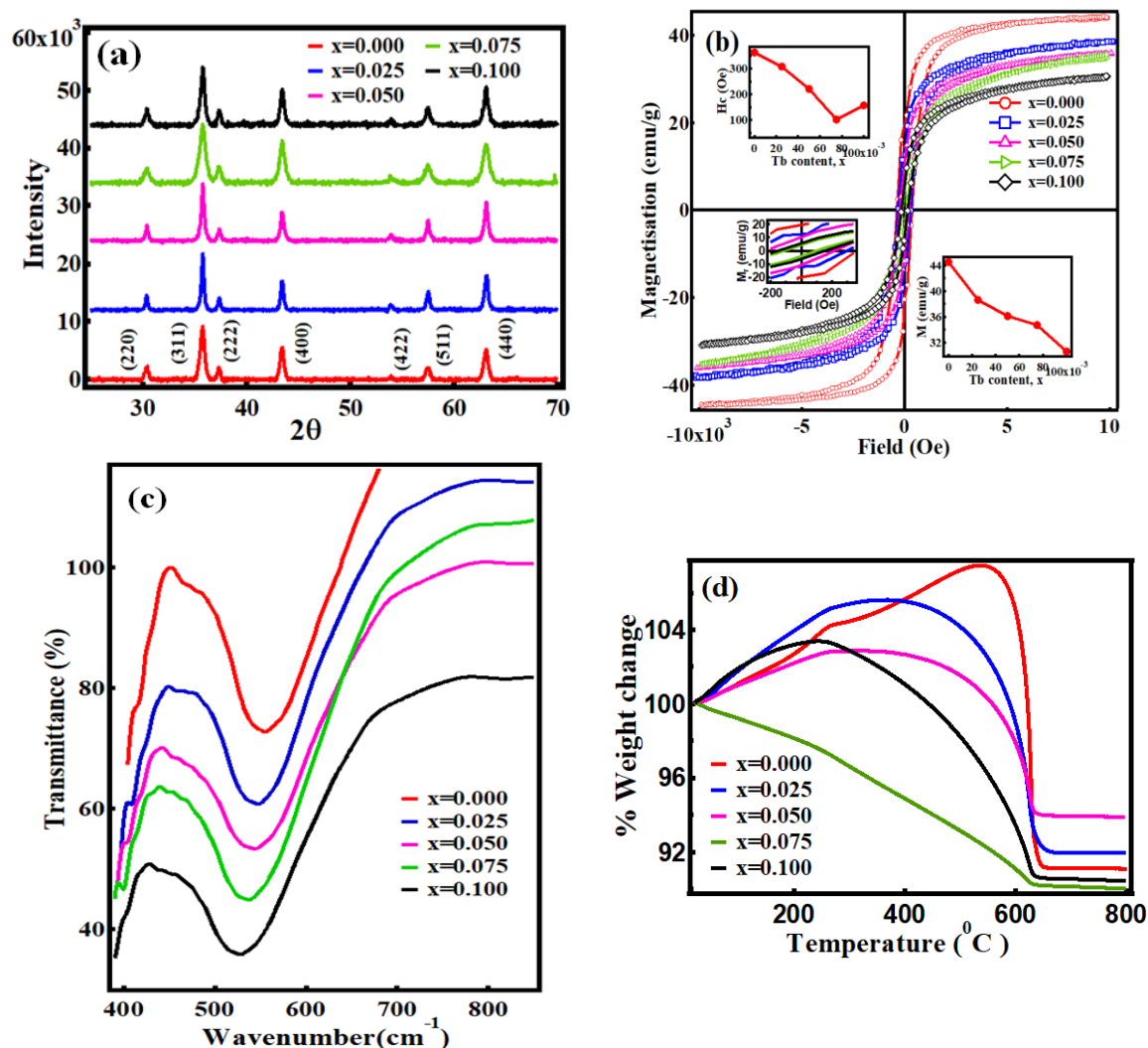


Figure 1. (a) X-ray diffraction (XRD) patterns of the $\text{NiTb}_x\text{Fe}_{2-x}\text{O}_4$ ($0.0 \leq x \leq 0.1$) nanoparticles. (b) Hysteresis loops at room temperature, M vs. H of $\text{NiTb}_x\text{Fe}_{2-x}\text{O}_4$. (c) Fourier transform infrared spectra of $\text{NiTb}_x\text{Fe}_{2-x}\text{O}_4$. (d) Thermogravimetric Analysis (TGA) curves of $\text{NiTb}_x\text{Fe}_{2-x}\text{O}_4$. TGA measurement was done in the presence of the magnetic field, thus the %Wt. change refers to the change in magnetic force.

Table 1. Values from the magnetic isotherms and Curie temperature, T_c , of $\text{NiTb}_x\text{Fe}_{2-x}\text{O}_4$.

x	M_s (emu/g)	M_r (emu/g)	M_r/M_s	H_c (Oe)	$K1 \times 10^5$ (5K) (J/m ³)	$K1 \times 10^5$ (300K) (J/m ³)	T_c (K)
0.000	44.5	19.8	0.44	363	3.9	2.5	938
0.025	38.6	11.9	0.30	308	8.3	5.7	923
0.050	36.1	10.8	0.29	221	6.3	5.6	913
0.075	34.7	8.6	0.25	102	10.1	6.5	903
0.100	30.6	6.2	0.20	157	10.9	6.3	899

The interionic distances (i.e., cation–anion distances at the A-site (d_{AL}) and B-site (d_{BL}), together with the distance of the closest anion–anion approach, tetrahedral edge, d_{AE} , and shared and unshared octahedral edges, d_{BE} , d_{BEU}) are calculated according to the following equations [27,28],

$$d_{AL} = a\sqrt{3}(u - 0.25), \quad (1)$$

$$d_{BL} = a(3u^2 - 11/4u + 43/64)^{1/2}, \quad (2)$$

$$d_{AE} = a\sqrt{2}(2u - 0.5), \quad (3)$$

$$d_{BE} = a\sqrt{2}(1 - 2u), \quad (4)$$

$$d_{BEU} = a(4u^2 - 3u + 11/16)^{1/2} \quad (5)$$

where u is the oxygen parameter ($u = 0.3811$ for NiFe_2O_4) [29]. Additionally, the distances L_A and L_B between the magnetic ions at the A-sites and B-sites (the jump length or hopping length), respectively, can be obtained where $L_A = a\sqrt{3}/4$, and $L_B = a\sqrt{2}/4$ [30]. Table 2 lists the calculated parameters. The values of d_{AL} , d_{BL} , d_{AE} , d_{BE} , d_{BEU} , and the hopping length, L_A and L_B , increases with Tb^{3+} content due to the replacement of smaller Fe^{3+} via larger radii ions Tb^{3+} in octahedral sites. The ionic radius of a rare-earth ion is larger than the tetrahedral site radii, and therefore energetics force the rare-earth ions to occupy octahedral sites. The preferred rare-earth occupancy for the octahedral site has been also corroborated by Mossbauer spectroscopy [16,20].

Table 2. Lattice parameters and Bond length of A-sites d_{AL} and B-sites d_{BL} , the tetrahedral edge d_{AE} , the shared and unshared octahedral edges, d_{BE} and d_{BEU} and the hopping length at A-site L_A and B-site L_B for $\text{NiTb}_x\text{Fe}_{2-x}\text{O}_4$ samples.

x	Lattice Parameter (Å)	Avg. Crystallite size (nm)	X-ray Density (g/cm^3)	d_{AL} (Å)	d_{BL} (Å)	d_{AE} (Å)	d_{BE} (Å)	d_{BEU} (Å)	L_A (Å)	L_B (Å)
0.000	8.3039(06)	36.41	5.44	1.8855	2.0265	3.0791	2.7926	2.9376	3.5956	2.9358
0.025	8.3076(04)	25.42	5.49	1.8864	2.0275	3.0805	2.7938	2.9389	3.5973	2.9371
0.050	8.3089(04)	22.49	5.55	1.8867	2.0278	3.0809	2.7942	2.9393	3.5979	2.9376
0.075	8.3093(02)	17.50	5.61	1.8868	2.0279	3.0811	2.7944	2.9395	3.5980	2.9378
0.100	8.3105 (05)	16.00	5.66	1.8870	2.0281	3.0815	2.7948	2.9399	3.5985	2.9382

Figure 1c shows the infrared absorption spectra of samples. The spectra show two distinct absorption bands with peaks at 554.3 (ν_1) cm^{-1} ($M_{\text{tetra}} \leftrightarrow \text{O}$ stretching) and 413.5 cm^{-1} (ν_2) ($M_{\text{octa}} \leftrightarrow \text{O}$ stretching). The band positions were found to agree with the characteristic infrared absorption bands of the AB_2O_4 type spinel [31]. The higher frequency band (ν_1) was found to shift from 554.3 cm^{-1} to 543.3 cm^{-1} while the lower frequency band (ν_2) shifted from 413.5 cm^{-1} to 406.2 cm^{-1} . Similar band shifting with the doping in NiFe_2O_4 has been reported in the literature [16,27,32,33]. The difference in the band positions is expected because of the difference in the Fe–O distances for the A and B sites. The Fe–O distance (1.89 Å) for the A site was smaller than that of a B site (1.99 Å) [34]. Thus, a high degree of covalency between Fe–O at the A site was expected, compared to that at the B site, which resulted in vibration stretching at higher wavenumbers. The increase in the site radius reduced the fundamental frequency, thus shifting the central frequency toward the lower frequency side [35]. Upon replacement of smaller Fe^{3+} ions by bigger Tb^{3+} ions, an increase in site radius is expected.

Figure 1b shows the room temperature (RT) hysteresis loops of the $\text{NiFe}_{2-x}\text{Tb}_x\text{O}_4$ samples measured in the ± 12 kOe field range. The inset in Figure 1b shows the saturation magnetization, M_s , and coercivity, H_c , as a function of Tb^{3+} content in $\text{NiFe}_{2-x}\text{Tb}_x\text{O}_4$. The hysteresis loop for NiFe_2O_4 exhibits saturation magnetization $M_s \sim 44.5$ emu/g, $M_r \sim 19.8$ emu/g, and the coercivity was ~ 363 Oe. The M_s value of the doped $\text{NiFe}_{2-x}\text{Tb}_x\text{O}_4$ samples decreased with the increase in Tb^{3+} content from 44.5 emu/g for $x = 0.0$ to 30.6 emu/g for $x = 0.1$. This reduction in M_s value could mainly arise from the replacement of magnetic Fe^{3+} with non-magnetic Tb^{3+} ions. An increase in the magnetization value at low temperature, at 60 kOe, for samples $x = 0.075$ and $x = 0.1$ could be attributed to the freezing of surface spin [36]. With the decrease in the crystallite size due to broken surface bond symmetry, the number of uncompensated spins was expected to increase. Later, upon freezing at low temperatures, they could align and hence increase the net magnetization of the particles [37]. Additionally, the saturation magnetization in ferrites has been observed to decrease with decreasing crystallite size due to the existence of spin canting in nanoparticles [38]. As discussed above, the spin canting originates from the finite-size and the surface effects. Additionally, the size effects in nanoparticles can cause a reduction in the magnetization values

compared with the bulk counterpart. Furthermore, the non-linear decrease in M_s value with Tb^{3+} may also result from the induced strain distorting bond angle ($Fe^{3+}-O^{2-}-Fe^{3+}$ (Tb^{3+})), which could weaken the superexchange interaction. Additionally, with the doping, $NiFe_{2-x}Tb_xO_4$ may move from a mixed spinel to inverse spinel structure [16,39], resulting in the large cancelation of moments between two sites. The H_C value of the $NiFe_{2-x}Tb_xO_4$ measured from the $M(H)$ loops at 300 K is shown in the inset of Figure 1b. The H_C value decreased with the Tb^{3+} content. The H_C value of ferrite NPs is reported to be sensitive to a synthesis method including heat treatment, particle size, and anisotropy constant. It is known that the effective anisotropy constant increases with decreasing particle sizes, as dictated by the expression for spherical nanoparticles as $K_{eff} = K_V + 6/d (K_s)$, where K_{eff} , K_V , and K_s denote the effective, volume, and surface anisotropy constants, respectively [40]. With the grain refinement upon Tb^{3+} substitution, the thermal energy becomes enough to overcome the volume-dependent anisotropy energy ($K_{eff}V$), enabling the easier reversal of the moments, thereby leading to the lower critical fields for these small-size nanoparticles [41,42]. This leads to a decrease in the coercivity of particles with increasing Tb^{3+} content. The squareness ratio value rapidly decreased from the 0.44 for $x = 0.0$ to 0.20 for $x = 0.1$ sample. According to the Stoner–Wohlfarth theory, the squareness ratio can take two values including one around 0.83 associated with the cubic anisotropy and another around 0.5 that corresponds to uniaxial anisotropy [43]. The squareness ratio value, $M_r/M_s \geq 0.5$ indicates that the particles are in the single magnetic domain, and those < 0.5 indicate particles with a multi-domain structure [35]. Furthermore, squareness ratio is a characteristic parameter of the prepared samples and depends on the anisotropy, indicating the ease with which the magnetization direction is reoriented to the nearest easy axis magnetization direction after the magnetic field is removed. The lower the M_r/M_s ratio value, the less anisotropic the material will be. The values of the M_r/M_s value ranges from 0.45 to 0.17 with increasing Tb^{3+} content from $x = 0$ to 0.1, Table 2. Additionally, the low value of M_r/M_s can be attributed to the increased fraction of superparamagnetic fraction and spin canting [44].

Isothermal magnetization, M , for the $NiFe_{2-x}Tb_xO_4$, is displayed in Figure 2a,b. Figure 2c shows the magnetization reduction with the temperature for all samples. The temperature-dependent reduction in magnetization could result from the breaking of ground state ferro/ferrimagnetic spin order by low energy excitations of the spins in the core and the disordered surface of ferromagnetic nanoparticles. The anisotropy constant, $K1$, for $NiFe_{2-x}Tb_xO_4$ samples were obtained from fitting the M vs. H data, Figure 2a,b to the expression [16], $M = M_s [1 - (8/105)(K1/M_s H)^2] = M_s(1 - \beta/H^2)$, where $\beta = (8/105)(K1/M_s)^2$, consequently, the slope of the linear fitting provides the constant β , which is related to the magnetocrystalline anisotropy constant $K1$, via, $K1 = M_s(105\beta/8)^{1/2}$. The numerical coefficient 8/105 holds for random polycrystalline samples with cubic anisotropy. The calculated value of $K1$ as a function of temperature for the $NiFe_{2-x}Tb_xO_4$ samples is plotted in Figure 2d and is listed in Table 2. The determined value of $K1$ for $NiFe_2O_4$ at 5 K was 3.90×10^5 J/m³, and at 300 K was 2.51×10^5 J/m³. These values agreed with the earlier reported $K1$ values measured at room temperature for nanocrystalline ferrites such as $CoFe_2O_4$ (2×10^6 J/m³), $MnFe_2O_4$ (3×10^4 J/m³), $NiFe_2O_4$ (0.7×10^5 J/m³), and Fe_3O_4 (0.9×10^5 J/m³) [45]. From Figure 2d, it is observed that the (1) $K1$ value decreases with the temperature, and (2) $K1$ increases with the Tb^{3+} content. The magnetocrystalline anisotropy depends on the crystalline field created by the ions in the environment of a given magnetic ion. While the magnetic anisotropy dictates the preferential alignment of spins along one direction and this magnetic anisotropy may originate for the sample shape, the stress, the surface structure of the grains, and by the crystalline structure of the grains. Higher $K1$ value was recorded for the Tb^{3+} doped samples at all temperatures in comparison to that of the undoped $NiFe_2O_4$ samples. Due to the so-called orbital quenching in the weak ligand field, transition metal oxides are marked by weak spin-orbit coupling [46,47]; however, the hybridization of Fe 3d-orbitals with O 2p-orbitals may occur if there are some distorted Fe-polyhedra in the non-ideal lattice [48,49]. Thus, the unquenched orbitals can increase magnetocrystalline anisotropy. This could possibly be the reason for the observed increase in $K1$ value in doped $NiFe_{2-x}Tb_xO_4$. Furthermore, surface anisotropy also adds to the effective anisotropy value with the grain refinement upon Tb^{3+} substitution [50]. The low-temperature $K1$

values are one order of magnitude larger than that at 300 K. This is indicative of the presence of inter-particle interaction, which is more marked for smaller particles that get unblocked at lower temperatures. However, the $K1$ value increases with Tb content. This increase in $K1$ could be related to the grain size reduction along with a reduction in M_s value due to magnetic dilution [51,52].

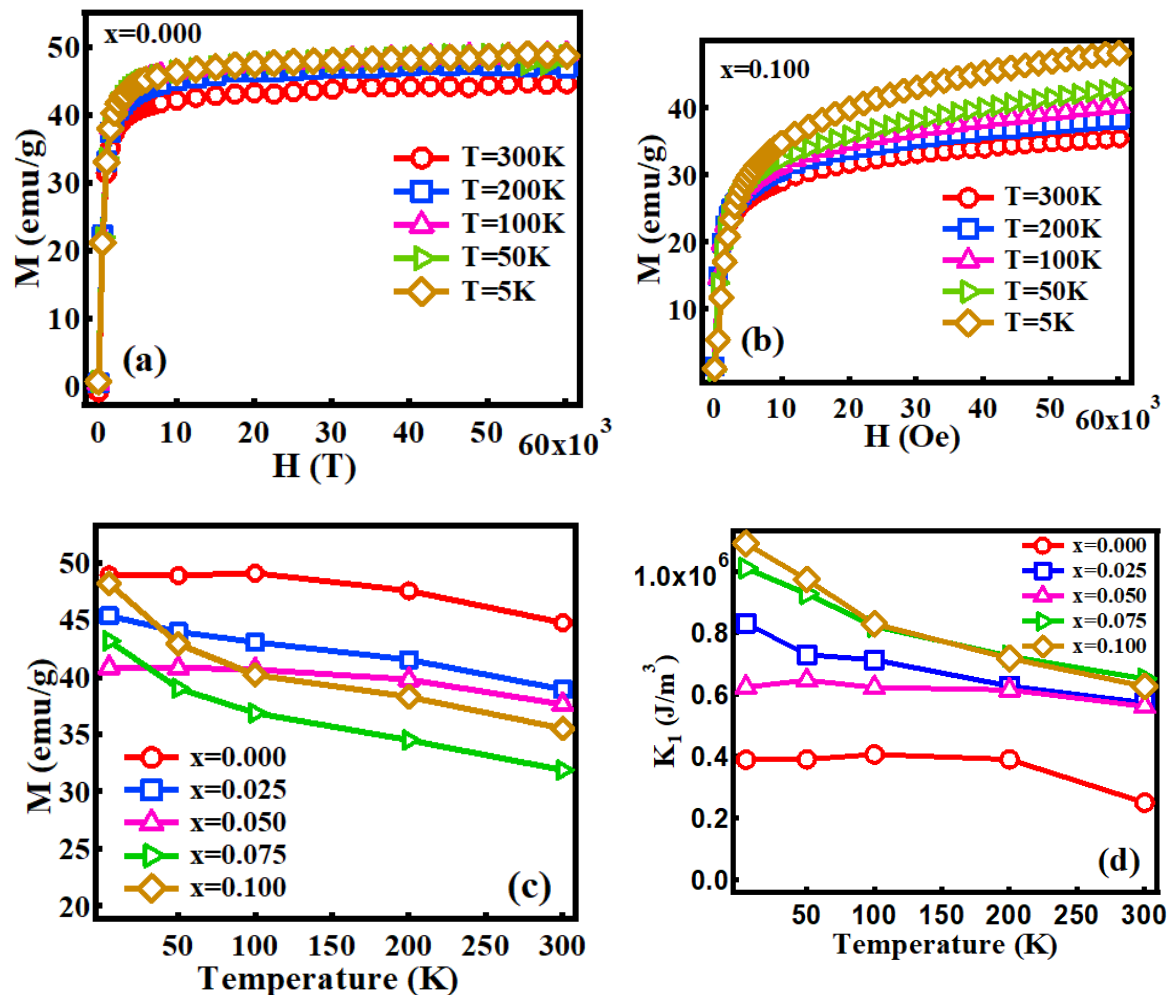


Figure 2. (a) Magnetic isotherms. (a) $x = 0.000$ and (b) $x = 0.100$ Tb^{3+} content in $\text{NiTb}_x\text{Fe}_{2-x}\text{O}_4$. (c) Magnetization vs. temperature curves as a function of Tb^{3+} content in $\text{NiTb}_x\text{Fe}_{2-x}\text{O}_4$ recorded at the 60 kOe field. (d) $K1$ obtained from fitting M vs. T using the law of approach to the saturation magnetization for $\text{NiTb}_x\text{Fe}_{2-x}\text{O}_4$ as a function of Tb^{3+} content.

The Curie temperature (Neel temperature for the ferrimagnetic system), T_c , of all samples is listed in Table 2. A decreasing trend in T_c was observed with the increase in Tb^{3+} content in $\text{NiFe}_{2-x}\text{Tb}_x\text{O}_4$, reaching a value of 899 K for $x = 0.1$, Figure 1d. The measured T_c of pure NiFe_2O_4 was ~ 938 K. Thus, an $\sim 6\%$ reduction for T_c was noticed for the $x = 0.1$ sample. This T_c reduction could result from (1) the decrease in the number of pairs of some super-exchange interactions due to the magnetic dilution effect; (2) spin canting; and (3) the strength of interaction due to the $\text{Fe}^{3+}-\text{O}^{2-}-\text{Fe}^{3+}$ bond angle deviation from the optimum angle for super-exchange interaction [53,54].

4. Summary

The substitution of a small amount of Tb^{3+} for Fe^{3+} affects the structural and magnetic properties of the ferrite. The substitution Fe^{3+} with larger ionic size Tb^{3+} leads to lattice expansion and possibly $\text{Fe}^{3+}-\text{O}^{2-}-\text{Fe}^{3+}$ bond angle distortion, which eventually weakens super-exchange interaction. The decrease in the M_s , M_r/M_s , and T_c is the result of the weakening of super-exchange interaction.

The substitution of Tb^{3+} at the B site was observed to improve magnetocrystalline anisotropy K_1 . On the other hand, K_1 decreased with the temperature. The effect of Tb^{3+} ion substitution in $NiFe_2O_4$ was to create a moderate reduction in M_s and T_c , but a significant reduction in coercivity. This makes the rare-earth-doped ferrite, $NiFe_{2-x}Tb_xO_4$, a better candidate for soft-magnetic applications such as inductor cores and high-frequency applications.

Author Contributions: Conceptualization, S.R.M. and D.G.; methodology, D.G. and T.P.P.; software, S.Y., B.K.R. and D.G.; validation, S.R.M., B.K.R. and S.Y.; formal analysis, S.R.M. and D.G.; investigation, S.R.M.; resources, S.R.M.; data curation, D.G. and S.C.B.; writing—original draft preparation, D.G.; writing—review and editing, S.R.M.; visualization, D.G.; supervision, S.R.M.; project administration, S.R.M.; funding acquisition, S.R.M. All authors have read and agreed to the published version of the manuscript.

Funding: This research received no external funding.

Conflicts of Interest: The authors declare no conflict of interest.

References

1. Pérez, E.; Marquez, G.; Sagredo, V. Effect of calcination on characteristics of nickel ferrite nanoparticles synthesized by sol-gel method. *Iraqi J. Appl. Phys.* **2019**, *15*, 13–17.
2. Dixit, G.; Negi, P.; Singh, J.P.; Srivastava, R.C.; Agrawal, H.M. Effect of Ce Doping on the Magnetic Properties of $NiFe_2O_4$ Nanoparticles. *J. Supercond. Nov. Magn.* **2013**, *26*, 1015–1019. [[CrossRef](#)]
3. Singhal, S.; Chandra, K. Cation distribution and magnetic properties in chromium-substituted nickel ferrites prepared using aerosol route. *J. Sol. State Chem.* **2007**, *180*, 296–300. [[CrossRef](#)]
4. Krishna, K.R.; Ravinder, D.; Kumar, K.V.; Lincon, C.A. Synthesis, XRD & SEM studies of zinc substitution in nickel ferrites by citrate gel technique. *World J. Cond. Matt. Phys.* **2012**, *2*, 153.
5. Dormann, J.L.; Nogues, M. Magnetic structures in substituted ferrites. *J. Phys. Cond. Matt.* **1990**, *2*, 1223. [[CrossRef](#)]
6. Rezlescu, N.; Rezlescu, E.; Pasnicu, C.; Craus, M.L. Effects of the rare-earth ions on some properties of a nickel-zinc ferrite. *J. Phys. Cond. Matt.* **1994**, *6*, 5707. [[CrossRef](#)]
7. Virden, A.E.; O'Grady, K. Structure and magnetic properties of NiZn ferrite nanoparticles. *J. Magn. Magn. Mater.* **2005**, *290*, 868–870. [[CrossRef](#)]
8. Batoo, K.M. Microstructural and Mössbauer properties of low temperature synthesized Ni-Cd-Al ferrite nanoparticles. *Nanoscale Res. Lett.* **2011**, *6*, 499. [[CrossRef](#)]
9. Sharma, R.K.; Suwalka, O.P.; Lakshmi, N.; Venugopalan, K. Hyperfine fields in nano particles of $Cr_{0.25}Co_{0.25}Zn_{0.5}Fe_2O_4$. *Indian J. Pure Appl. Phys.* **2007**, *45*, 830–833.
10. Wang, L.; Rai, B.K.; Mishra, S.R. Structural and magnetic study of Al^{3+} doped $Ni_{0.75}Zn_{0.25}Fe_{2-x}Al_xO_4$ nanoferrites. *Mater. Res. Bull.* **2015**, *65*, 183–194. [[CrossRef](#)]
11. Borhan, A.I.; Iordan, A.R.; Palamaru, M.N. Correlation between structural, magnetic and electrical properties of nanocrystalline Al^{3+} substituted zinc ferrite. *Mater. Res. Bull.* **2013**, *48*, 2549–2556. [[CrossRef](#)]
12. Hashim, M.; Kumar, S.; Ali, S.; Koo, B.H.; Chung, H.; Kumar, R. Structural, magnetic and electrical properties of Al^{3+} substituted Ni–Zn ferrite nanoparticles. *J. Alloy. Compd.* **2012**, *511*, 107–114. [[CrossRef](#)]
13. Lakhani, V.K.; Zhao, B.; Wang, L.; Trivedi, U.N.; Modi, K.B. Negative magnetization, magnetic anisotropy and magnetic ordering studies on Al^{3+} -substituted copper ferrite. *J. Alloy. Compd.* **2011**, *509*, 4861–4867. [[CrossRef](#)]
14. Lakhani, V.K.; Pathak, T.K.; Vasoya, N.H.; Modi, K.B. Structural parameters and X-ray Debye temperature determination study on copper-ferrite-aluminates. *Solid State Sci.* **2011**, *13*, 539–547. [[CrossRef](#)]
15. Sharifi, I.; Shokrollahi, H. Structural, magnetic and Mössbauer evaluation of Mn substituted Co–Zn ferrite nanoparticles synthesized by co-precipitation. *J. Magn. Magn. Mater.* **2013**, *334*, 36–40. [[CrossRef](#)]
16. Poudel, T.P.; Rai, B.K.; Yoon, S.; Guragain, D.; Neupane, D.; Mishra, S.R. The effect of gadolinium substitution in inverse spinel nickel ferrite: Structural, Magnetic, and Mössbauer study. *J. Alloy. Compd.* **2019**, *802*, 609–619. [[CrossRef](#)]
17. Jacob, B.P.; Kumar, A.; Pant, R.P.; Singh, S.; Mohammed, E.M. Influence of preparation method on structural and magnetic properties of nickel ferrite nanoparticles. *B. Mater. Sci.* **2011**, *34*, 1345–1350. [[CrossRef](#)]

18. Sontu, U.B.; Yelasani, V.; Musugu, V.R.R. Structural, electrical and magnetic characteristics of nickel substituted cobalt ferrite nano particles, synthesized by self combustion method. *J. Magn. Magn. Mater.* **2015**, *374*, 376–380. [[CrossRef](#)]
19. Almessiere, M.A.; Slimani, Y.; Güngüneş, H.; Ali, S.; Manikandan, A.; Ercan, I.; Baykal, A.; Trukhanov, A.V. Magnetic attributes of NiFe₂O₄ nanoparticles: Influence of dysprosium Ions (Dy³⁺) substitution. *Nanomaterials* **2019**, *9*, 820. [[CrossRef](#)]
20. Cheng, F.X.; Jia, J.T.; Xu, Z.G.; Zhou, B.; Liao, C.S.; Yan, C.H.; Chen, L.Y.; Zhao, H.B. Microstructure, magnetic, and magneto-optical properties of chemical synthesized Co-RE (RE= Ho, Er, Tm, Yb, Lu) ferrite nanocrystalline films. *J. Appl. Phys.* **1999**, *86*, 2727–2732. [[CrossRef](#)]
21. Morrish, A.H. The physical principles of magnetism. In *The Physical Principles of Magnetism*; Morrish, A.H., Ed.; Wiley-VCH: Hoboken, NJ, USA, 2001; p. 696.
22. Bharathi, K.K.; Chelvane, J.A.; Markandeyulu, G. Magnetoelectric properties of Gd and Nd-doped nickel ferrite. *J. Magn. Magn. Mater.* **2009**, *321*, 3677–3680. [[CrossRef](#)]
23. Şabikoğlu, İ.; Paralı, L.; Malina, O.; Novak, P.; Kaslik, J.; Tucek, J.; Pechousek, J.; Navarik, J.; Schneeweiss, O. The effect of neodymium substitution on the structural and magnetic properties of nickel ferrite. *Prog. Nat. Sci. Mater.* **2015**, *25*, 215–221. [[CrossRef](#)]
24. Lueken, H. *Course of Lectures on Magnetism of Lanthanide Ions under Varying Ligand and Magnetic Fields*; Institute of Inorganic Chemistry, RWTH Aachen: Aachen, Germany, 2008.
25. Jacob, B.P.; Thankachan, S.; Xavier, S.; Mohammed, E.M. Effect of Tb³⁺ substitution on structural, electrical and magnetic properties of sol-gel synthesized nanocrystalline nickel ferrite. *J. Alloy. Compd.* **2013**, *578*, 314–319. [[CrossRef](#)]
26. Smith, J.; Wijn, H.P.J. *Ferrites*; John Wiley: New York, NY, USA, 1959.
27. Pandit, A.A.; More, S.S.; Dorik, R.G.; Jadhav, K.M. Structural and magnetic properties of Co_{1+y}Sn_yFe_{2-2y-x}Cr_xO₄ ferrite system. *B Mater. Sci.* **2003**, *26*, 517–521. [[CrossRef](#)]
28. Abbas, T.J. X-ray Diffraction and Site Preference Analysis of Ni-Substituted MgFe₂O₄ Ferrites. *J. Appl. Sci.* **2002**, *2*, 1110–1114.
29. Wohlfarth, E.P. *Ferromagnetic Materials*; North-Holland Publication Co.: Amsterdam, The Netherlands, 1982.
30. Dhiman, R.L.; Taneja, S.P.; Reddy, V.R. Preparation and Characterization of Manganese Ferrite Aluminates. *Adv. Condens. Matter Phys.* **2008**, *7*. [[CrossRef](#)]
31. Waldron, R.D. Infrared spectra of ferrites. *Phys. Rev.* **1955**, *99*, 1727. [[CrossRef](#)]
32. Hemeda, O.M.; Barakat, M.M.; Hemeda, D.M. Structural, Electrical and Spectral Studies on Double Rare-Earth Orthoferrites La_{1-x}Nd_xFeO₃. *J. Turk. Phys.* **2003**, *27*, 537.
33. Shinde, T.J.; Gadkari, A.B.; Vasambekar, P.N. Influence of Nd³⁺ substitution on structural, electrical and magnetic properties of nanocrystalline nickel ferrites. *J. Alloy. Compd.* **2012**, *513*, 80–85. [[CrossRef](#)]
34. Evans, B.J.; Hafner, S.S. Mössbauer resonance of Fe⁵⁷ in oxidic spinels containing Cu and Fe. *J. Phys. Chem. Solids* **1968**, *29*, 1573–1588. [[CrossRef](#)]
35. Modi, K.B.; Rangolia, M.K.; Chhantbar, M.C.; Joshi, H.H. Study of infrared spectroscopy and elastic properties of fine and coarse grained nickel-cadmium ferrites. *J. Mater. Sci.* **2006**, *41*, 7308–7318. [[CrossRef](#)]
36. Kodama, R.H.; Berkowitz, A.E.; McNiff, E.J., Jr.; Foner, S. Surface spin disorder in NiFe₂O₄ nanoparticles. *Phys. Rev. Lett.* **1996**, *77*, 394–397. [[CrossRef](#)] [[PubMed](#)]
37. Berkowitz, A.E.; Kodama, R.H.; Makhlof, S.A.; Parker, F.T.; Spada, F.E.; McNiff, E.J., Jr.; Foner, S. Anomalous properties of magnetic nanoparticles. *J. Magn. Magn. Mater.* **1999**, *196*, 591–594. [[CrossRef](#)]
38. Hemeda, O.M.; Said, M.Z.; Barakat, M.M. Spectral and transport phenomena in Ni ferrite-substituted Gd₂O₃. *J. Magn. Magn. Mater.* **2001**, *224*, 132–142. [[CrossRef](#)]
39. Šepelák, V.; Baabe, D.; Mienert, D.; Schultze, D.; Krumeich, F.; Litterst, F.J.; Becker, K.D. Evolution of structure and magnetic properties with annealing temperature in nanoscale high-energy-milled nickel ferrite. *J. Magn. Magn. Mater.* **2003**, *257*, 377–386. [[CrossRef](#)]
40. Bødker, F.; Mørup, S.; Linderroth, S. Surface effects in metallic iron nanoparticles. *Rev. Lett.* **1994**, *72*, 282. [[CrossRef](#)]
41. Pfeiffer, H. Determination of anisotropy field distribution in particle assemblies taking into account thermal fluctuations. *Phys. Status solidi A* **1990**, *118*, 295–306. [[CrossRef](#)]
42. Vestal, C.R.; Zhang, Z.J. Synthesis and magnetic characterization of Mn and Co spinel ferrite-silica nanoparticles with tunable magnetic core. *Nano. Lett.* **2003**, *3*, 1739–1743. [[CrossRef](#)]

43. Stoner, E.C.; Wohlfarth, E.P. Philos. Handbook of Nanomaterials for Industrial Applications. *T. R. Soc. S-A* **1948**, *240*, 599–642.
44. Jiang, J.Z.; Goya, G.F.; Rechenberg, H.R. Magnetic properties of nanostructured CuFe_2O_4 . *J. Phys. Condens Mat.* **1999**, *11*, 4063. [[CrossRef](#)]
45. Robert, C.O.; Handley, O. *Modern Magnetic Materials: Principles and Applications*; John Wiley & Sons, Inc.: New York, NY, USA, 2000.
46. Merer, A.J. Spectroscopy of the diatomic 3d transition metal oxides. *Annu. Rev. Phys. Chem.* **1989**, *40*, 407–438. [[CrossRef](#)]
47. Ham, F.S. Dynamical Jahn-Teller effect in paramagnetic resonance spectra: Orbital reduction factors and partial quenching of spin-orbit interaction. *Phys. Rev.* **1965**, *138*, A1727–A1740. [[CrossRef](#)]
48. Kim, J.Y.; Koo, T.Y.; Park, J.H. Orbital and bonding anisotropy in a half-filled GaFeO_3 magnetoelectric ferrimagnet. *Phys. Rev. Lett.* **2006**, *96*, 047205–047209. [[CrossRef](#)] [[PubMed](#)]
49. Arima, T.; Higashiyama, D.; Kaneko, Y.; He, J.P.; Goto, T.; Miyasaka, S.; Kimura, T.; Oikawa, K.; Kamiyama, T.; Kumai, R.; et al. Structural and magnetoelectric properties of $\text{Ga}_{2-x}\text{Fe}_x\text{O}_3$ single crystals grown by a floating-zone method. *Phys. Rev. B* **2004**, *70*, 064426. [[CrossRef](#)]
50. Yoon, S.; Krishnan, K.M. Temperature dependence of magnetic anisotropy constant in manganese ferrite nanoparticles at low temperature. *J. Appl. Phys.* **2011**, *109*, 07B534. [[CrossRef](#)]
51. Shenker, H. Magnetic anisotropy of cobalt ferrite ($\text{Co}_{1.01}\text{Fe}_{2.00}\text{O}_{3.62}$) and nickel cobalt ferrite ($\text{Ni}_{0.72}\text{Fe}_{0.20}\text{Co}_{0.08}\text{Fe}_2\text{O}_4$). *Phys. Rev.* **1957**, *107*, 1246. [[CrossRef](#)]
52. Gao, R.W.; Feng, W.C.; Liu, H.Q.; Wang, B.; Chen, W.; Han, G.B.; Zhang, P.; Li, H.; Li, W.; Guo, Y.Q.; et al. Exchange-coupling interaction, effective anisotropy and coercivity in nanocomposite permanent materials. *J. Appl. Phys.* **2003**, *94*, 664–668. [[CrossRef](#)]
53. Gilleo, M.A. Superexchange interaction energy for $\text{Fe}^{3+}\text{-O}^{2-}\text{-Fe}^{3+}$ linkages. *Phys. Rev.* **1958**, *109*, 777. [[CrossRef](#)]
54. Goldman, A. *Modern Ferrite Technology*; Van Nostrand Reinhold: New York, NY, USA, 1990; p. 145.



© 2020 by the authors. Licensee MDPI, Basel, Switzerland. This article is an open access article distributed under the terms and conditions of the Creative Commons Attribution (CC BY) license (<http://creativecommons.org/licenses/by/4.0/>).